ELASTIC MICROSTRAINS DURING TENSION AND
CREEP OF SUPERALLOYS: RESULTS FROM IN SITU NEUTRON DIFFRACTION

Y. Lu[1], S. Ma[2], and B.S. Majumdar[3*]
[1] Currently at Rice University, Houston, Florida
[2] Currently at University of Michigan, Ann Arbor, MI 48103
[3] Materials Department, New Mexico Tech, Socorro, NM 87801
[*] Corresponding Author, majumdar@nmt.edu

Keywords: Microstrain, neutron diffraction, internal stress, misfit, resolved shear stress, CRSS

ABSTRACT

In situ neutron diffraction experiments were conducted to monitor *elastic* microstrains during tension and creep of a directionally solidified (DS) superalloy PWA1422 and a single crystal (SX) alloy PWA 1484. The rationale was to obtain insight on internal stress evolution, and thereby improved understanding of deformation mechanisms. The misfit between the gamma (γ) and gamma-prime (γ') phases were determined as a function of temperature and deformation. The microstrains in the tension test were used to obtain the critical resolved shear stress (CRSS) of the phases. Results show a dramatic increase in the CRSS of the γ-phase compared to the bulk, and are consistent with dislocations bowing (Orowan type) between narrow γ-channels. A threshold stress is calculated for dislocation activity in the horizontal channel, and is suggested as a minimum stress for initiating any creep or rafting. Microstrains from the creep test at 900°C/425 MPa are consistent with the formation of dislocation networks, but the data do not suggest that the CRSS is exceeded for cutting of the γ'. Rather, rafting is suggested for the onset of tertiary creep. At 1092°C/120 MPa, the far-field creep strain exhibits an unusual behavior in the pre-steady-state low strain (<0.5%) regime. This is also accompanied with creep acceleration and decrease of elastic strain in γ'. The response is accompanied with the formation of a completely rafted microstructure. An explanation is provided in terms of deposition of actual misfit dislocations preferentially on the vertical interfaces.

1. INTRODUCTION

Current high performance turbine blades in aircraft engines are mostly fabricated with DS or SX Ni-base superalloys, which contain a high volume fraction (V_f>0.6) of γ' phase (ordered fcc, $L1_2$) coherently embedded in a disordered fcc γ matrix. The high yield strength of the alloy is believed to arise from the difficulty of penetration of dislocations into the γ' precipitates, coupled with the high constraint imposed on the relatively weak matrix γ channels of only 40-80 nm width [1]. Understanding the constraint effect is important for new high performance materials based on nanoscale structures. In addition, improved understanding of the mechanisms that lead to tertiary creep are important for developing alloys with improved creep resistance at homologous temperatures approaching 0.9 and above.

Although significant research has been conducted on DS and SX superalloys, there still remains a lack of clarity regarding internal stress evolution and precise deformation mechanisms at the nanoscale γ and γ' level. The onset of dislocation motion is different in the horizontal and vertical channels because of misfit stresses. In addition, the *in situ* critical resolved shear stresses (CRSS) of the phases are not known. The γ' phase directly participates in plastic deformation only at high stresses, when the resolved shear stress (RSS) is sufficient to allow the ingress of pairs of dislocations into the γ' phase from the γ phase. At high temperature, the cutting of the γ' phase would lead to high creep rates, so that much of the useful creep life of high V_f alloys is spent prior to cutting of the γ' phase. While γ' cutting has been observed in a number of studies following the onset of tertiary creep, it is important to ascertain that the local stress conditions in the γ' are compatible with its CRSS. In addition, the mere observation of dislocations inside the γ' phase may not provide a complete picture about the onset of tertiary creep; i.e., their density and velocity must be consistent with observed creep rates. Complicating the creep scenario is the formation of rafts during creep, which occur at temperatures of 900°C and above. Although their formation is ascribed to a minimum level of dislocation activity [2-4] and different strain energies in the horizontal and vertical channels [5,6], the changes in the internal stresses that accompany their formation, as well as the subsequent mechanisms by which they influence tertiary creep, are not clearly understood.

The rafting issue is particularly important at temperatures of 1000°C and above at low stresses (~100 - 150 MPa). Indeed, considerable recent research is devoted to understanding the effects of misfit (often negative) in this regime on the onset of tertiary creep, and how strains are accomplished after the microstructure has fully rafted [7,8]. It is also not clear if sliding may occur at the γ/γ' interface and thereby contribute to the onset of tertiary creep above 900°C. If interface dislocations are interpreted as implying partial or full loss of coherency [9], so that vacancy emission and absorption become easier at the interface [10], then interface sliding can occur and contribute to higher creep rate. A direct proof of sliding at the interface, such as using line markers, poses an extremely challenging task. However, measurements of local elastic strains and stresses, combined with modeling, may provide indirect evidence regarding sliding as a contributing factor.

The above deficiencies in the current knowledge base of superalloys formed the rationale for the work conducted here. *In situ* neutron diffraction experiments were conducted under tensile and creep loading conditions to determine the CRSS of the phases and obtain insight on how internal elastic strains and stresses evolve as a function of deformation. Tests were conducted on a [001] oriented PWA1422 DS alloy (no Re) at 900°C, and on a PWA 1484 SX alloy (3 wt.% Re) at 1092 C. The tests were

accompanied with micromechanical modeling and TEM observation of dislocation structures, although some of these details will not be presented in this paper. Publications related to this work may be obtained from [11-13].

2. EXPERIMENTS

The PWA 1422 DS alloy had the chemical composition: 58.32Ni-9.91Co-8.80Cr-12.42W-4.86Al-1.98Ti-1.03Nb-2.45Hf-0.14C-0.016B-0.077Zr, wt.%, and is similar to MAR M-200 alloy. The initial rods were about 20 mm diameter, with the rod axis aligned nominally along the [001] direction. The SX PWA1484 alloy is a 2nd generation alloy, very similar to CMSX-4, and had the chemical composition: 59.1Ni-10Co-5Cr-6W-5.6Al-2Mo-9Ta-0.3Hf-3Re wt.%. The castings were subjected to a solution heat treatment at 1260 °C in vacuum followed by rapid cooling. The samples were subsequently heat treated in an argon environment at 1079 °C/4 hours, followed by rapid cooling in air.

For the metallographic analysis, a technique that worked particularly well was to preferentially electroetch the γ phase in a 3 percent phosphoric acid solution at RT for 8 hours at an imposed voltage of 3 V. This technique was effective in revealing the 3D morphology of the γ′ phase. TEM samples were prepared perpendicular to the loading axis.

Tensile tests were conducted *in situ* on the superalloy samples at the Lujan Neutron Scattering Center (LANSCE) facility at Los Alamos, on their SMARTS (Spectrometer for Materials Research at Temperature and Stress) spectrometer. Here, a pulsed neutron diffraction source is used to interrogate a sample under stress and up to very high temperatures, while the specimen is held in a vacuum environment. A horizontal sevohydraulic loading frame is used to apply mechanical load either in load or displacement control. Figure 1 shows the experimental set up.
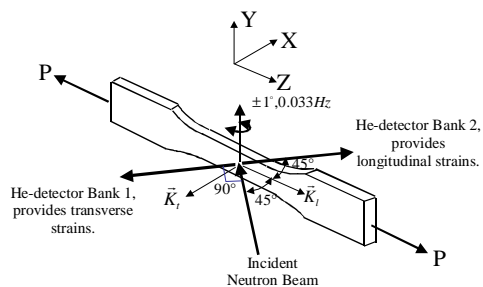

Figure 1. Schematic of the experimental setup. The sample is oscillated ±1° about the laboratory Y-axis which is perpendicular to the plane in which the incident and scattered beams lie.

The SMARTS facility utilizes polychromatic neutrons from a pulsed spallation source (wavelength, λ, typically in the range of 1-8 A°), with the collimated neutron beam impinging on the sample at 45 degree to the loading axis. A set of two He detectors are positioned at right angles to the incident beam, such that Banks 1 and 2 detect neutrons with scattering vectors perpendicular and parallel to the loading axis, respectively. The time-of-flight (TOF) of neutrons is converted to wavelength using DeBroglie's equation, since the distance of flight (flight path) and TOF are known.

Note that the detectors are held fixed at 2θ of +90 and –90°, respectively, with respect to the incident beam. As a result, the

parameters that are changing in the Bragg equation ($\lambda=2d_{hkl}sin\theta$) are λ and plane spacing, d_{hkl}. Tensile and creep tests were conducted at a number of temperatures. In this paper, we report on tensile and creep (425 MPa) test of the DS alloy at 900°C, and a creep test on the SX alloy at 1092°C at nominally 120 MPa stress. During the *in situ* tensile tests, the load or strain was held constant at different load levels for 20 minutes during which time neutron data were collected and binned for d_{hkl} calculations. During the creep tests at constant load, the data were binned for every 15 minutes and the total counts during this interval were used for diffraction analysis.

A major advantage of the SMARTS facility at LANSCE is that the loading frame is mounted on a pedestal that can be rotated about a vertical Y-axis (Fig.1). This allows the specimen axis to be aligned at any angle with respect to the incoming beam. In most standard test procedures, this angle is kept fixed at 45°. In order to compensate for possible loss of data due to specimen misalignment, the pedestal was oscillated about the laboratory Y-axis by ±1° about the mean 45° angle at a slow rate of approximately 0.033 Hz. Analysis of diffraction data showed that this approach was able to enhance neutron detection significantly.

3. RESULTS AND ANALYSIS

Figure 2 shows micrographs of the SX PWA1484 alloy. The micrographs confirm that the samples had good [001] alignment. Fig.2c illustrates the γ′ morphology following preferential dissolution of the γ-phase, and the technique is particularly useful for observing rafted microstructures. From the high magnification SEM micrographs as well as TEM, the Vf of the γ′ phase in the SX alloy was 0.67. The V_f for the DS alloy was 0.65. TEM micrographs showed that the size of the γ′ phase ranged between 370 and 430 nm, while the γ channel width ranged between 60 and 80 nm.
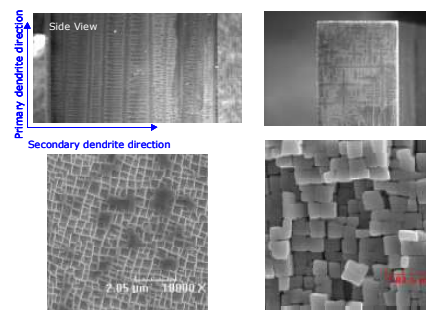

Figure 2. Clockwise from top left: (a) macroetched sample showing primary dendrites along tensile axis as well as secondary dendrites; (b) macroetched cross-section with secondary and tertiary dendrites; (c) electro-etched microstructure showing γ/γ′ phases; white lines indicate γ-phase; (d) preferentially dissolved γ, showing 3-D morphology of the remaining γ′ cubes.

Figure 3 shows the typical neutron diffraction spectrum obtained from the DS superalloy, with the intensity (arbitrary units) plotted versus the d-spacing. The Rietveld refinement technique [14] is used to analyze the neutron spectrum using the General Structures and Analysis System (GSAS) code developed by Larson and Von Dreele [15,16] at the Los Alamos Neutron Scattering Center (LANSCE). For the DS and SX superalloy

loaded along [001], only {h00} peaks are obtained. Therefore, we relied only on the single peak fitting procedure in GSAS for each peak [15,16], concentrating on the (100) peak for the γ' and the (200) peak for the γ+γ' phases.

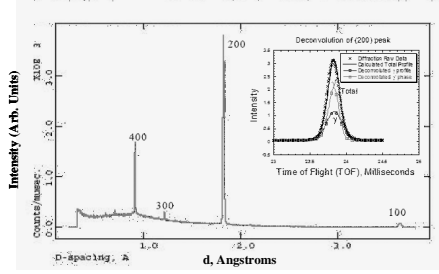

Figure 3. A typical neutron diffraction spectrum from Bank 2 with intensity plotted versus d-spacing. The inset shows the deconvoluted γ (lower) and γ' (upper) peaks.

In the single-fit approach, the superlattice (100) reflection is used to determine d_{100} for the γ' phase. For the corresponding (200) reflection, that includes intensity from both the γ' and γ phases, d_{200} of γ' was equated to $d_{100}/2$. The intensity ratio of γ' to γ was determined from the structure factor and volume fraction, using equation below [11]:

$$\frac{I^{\gamma'}_{2h2k2l}}{I^{\gamma}_{2h2k2l}} = \frac{\left|F^{\gamma'}_{2h2k2l}\right|^2}{\left|F^{\gamma}_{2h2k2l}\right|^2}\frac{v^{\gamma'}_f}{(1-v^{\gamma'}_f)} \tag{1}$$

where $F_{hkl} = b_c e^{2\pi i(h.0+k.0+l.0)} + b_f\left[e^{2\pi i(0.5h+0.5k+0l)} + e^{2\pi i(0.5h+0k+0.5l)} + e^{2\pi i(0h+0.5k+0.5l)}\right]$

where b_c and b_f are the scattering lengths of the corner atoms and face atoms, respectively, F_{hkl} is the structure factor, and V_f is the volume fraction of the γ' phase. In the case of the γ' phase, F_{2h2k2l} becomes equal to $(b_c + 3b_f)$, whereas for the γ phase it is simply $4b_g$, where b_g is the scattering length of the atom in the γ phase. In order to account for the actual composition of the phases, we calculated equivalent b_c and b_f using composition estimates of the γ and γ' phases using scattering lengths [17] and partition functions in [18-20]. The inset in Fig. 3 shows the (200) peak profile with TOF axis, along with the deconvoluted γ and γ' peaks.

The lattice misfit, δ { $= 2(a_{\gamma'}-a_g)/(a_{\gamma'}+a_{\gamma})$ }, were calculated based on our single-fit calculation of the (100) and (200) peaks. Since the lattice parameters were measured in the constrained condition where the phases are mutually strained elastically to maintain coherency, the δ refers to the constrained misfit.

The misfit data for the DS PWA1422 alloy is plotted in Fig. 4, along with results from other investigations.
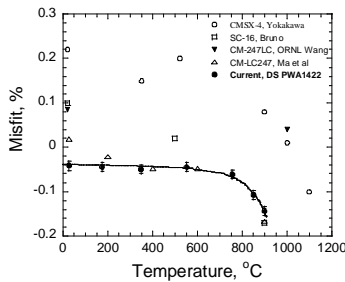

Figure 4. Plot of lattice misfit, δ, in percent, versus temperature. for DS PWA1422, as well as data on similar alloys.

Note that the misfit for the DS alloy remains fairly constant from RT to about 750 °C, and then decreases more

rapidly. At RT, the lattice parameter of the γ' powder extracted from this alloy indicated negligible difference with the γ' in the bulk, so that RT could be considered as free of misfit stress [13,21]. A very similar behavior was observed for the SX PWA1484 alloy, with the misfit remaining close to zero up to 600 C, and then increasing to -0.0013 at 900°C and -0.003 at 1092°C [21]. Lattice parameter measurements on the γ' powder extracted from this SX alloy showed less than 0.001 A° difference from that of the γ' in the bulk from RT to 600°C. This suggests that the SX alloy was essentially free of misfit stress up to about 600°C. It has been suggested [22] that the rapid increase in the magnitude of misfit at the high temperatures may be related to the re-dissolution of some of the γ' forming elements, such that the γ phase can equilibrate to its most stable composition. Although not shown here, our measurements also indicate that the thermal expansion of γ (not γ') is largely responsible for the sharp increase in misfit above 600 -750 °C [21].

3.1 Tension Test of DS Alloy at 900°C

The loading history of the sample tension tested at 900 °C is shown in Figure 5a. The sample was loaded in steps up to a maximum applied stress (σ_a) of approximately 700 MPa, by which time the sample had plastically yielded to a total strain of nearly 8%. The loading was performed under load control up to 350 MPa. During the hold periods, some creep started to be observed at a stress as low as 150 MPa, and this became really noticeable at 350 MPa. In order to prevent excessive creep, the sample was held at constant actuator displacement during the 20-minute neutron capture at stresses above 350 MPa. Time dependent stress relaxation during hold occurred at these higher stresses, and these may be observed in Fig.5a. The stress relaxation behavior is illustrated in Fig. 5b by regions T (top) to B (bottom), where the far-field extensometer strain is plotted on the x-axis.
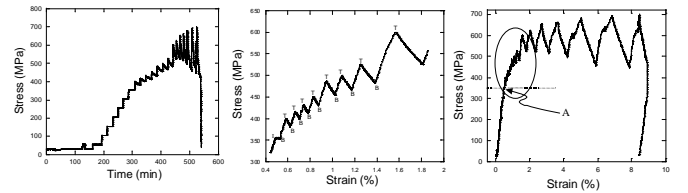

Figure 5. (a) Strain-time history of the tensile test of DS alloy at 900°C. (b) Stress-strain plot of the same specimen, where stress relaxation occurs from T to B. (c) Same data showing the overall behavior up to large strain.

Figure 5c shows that the stress-strain behavior is linear up to about 350 MPa (point A) beyond which there is appreciable non-linearity. However, point A should not be interpreted as macroscopic yielding of the DS alloy under typical tension test conditions. During each loading step between 350 and nearly 550 MPa (from B to T in Fig.5b), the load increased almost linearly from B to T. The slope ($d\sigma/d\varepsilon$) during the loading step was the same as before 350 MPa, and corresponded to the elastic modulus of the material. If macroscopic plasticity had occurred during loading, the slope from B to T would not be constant.

If the stress-strain segments of Fig. 5b or 5c are horizontally shifted by overlapping of the loading segments from B to T, and removing the decay segments T to B, then the overall stress-strain plot looks similar to a regular stress-strain plot [13]. In this way, microplasticity is observed to initiate at approximately 550 MPa.

The macroscopic estimated 0.2% offset yield strength is about 625 MPa. The yield strengths from tensile tests based on standard ASTM test procedures is 670 MPa at 900 °C. Thus, the estimated yield strength of 625 MPa is in reasonable agreement with standard tensile test results. Finally, the elastic modulus of the [001] oriented DS superalloy was determined to be 98 GPa.

The lattice parameters of the γ and γ′ were used to determine the elastic strains in the phases {$\varepsilon = (a-a_0)/a_o$}, where a and a_o are the instantaneous and initial lattice parameters, respectively. In our elastic strain plots, the initial lattice parameters (a_o) for the two phases correspond to those at 900 °C at nominally zero stress. Thus, the calculated elastic strains do not include the misfit strain.

Figures 6a and 6b show the phase specific elastic strains as a function of applied stress along the longitudinal and transversal direction, respectively. The error in strain was ±0.0001. Below 350 MPa, both the γ and γ′ show a linear relationship between the applied stress and elastic strain. From the elastic region in Figure 9a, we obtain E = 98 GPa for both the γ and γ′, in good agreement with that from extensometer data. The saturation of the elastic strain in the γ phase beyond point A is believed to be due to stress relaxation in the γ channels through thermally activated dislocation motion, such that stress in the γ phase cannot increase any further. Although very small creep was observed during hold at 150 MPa, the stress relaxation in γ was small, and non-linearity of elastic strain in γ became noticeable only at 350 MPa.
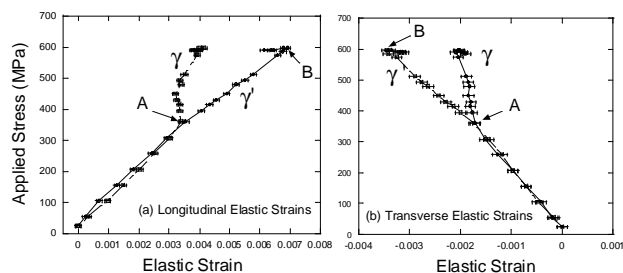
Figure 6. Phase-specific elastic strains in DS alloy: (a) longitudinal, and, (b) transverse direction, as a function of applied stress, during tensile test at 900°C.
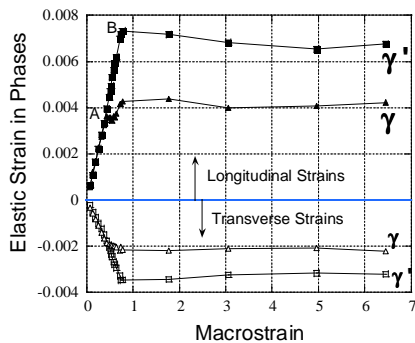
Figure 7. Phase-specific elastic strains in DS alloy at 900°C, as a function of far-field extensometer strain.

Figure 7 shows the elastic strain data plotted as a function of far-field strain measured using the extensometer. This plot clearly shows that the material is fully in the plastic regime, following point B in Fig. 6. Note that the elastic strains retain a fairly constant value during this period of plastic deformation.

TEM images were obtained for a separate sample that was unloaded at a total strain of 0.9 %, corresponding slightly to the right of point B in Fig.7. The sample was sectioned with a surface normal along the loading direction and thus represents a cross-section sample.
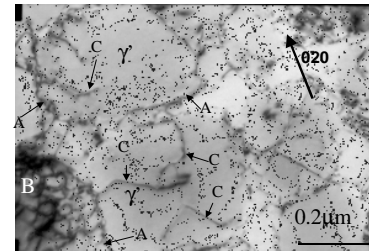
Figure 8. Bright field TEM image from 900 °C tensile tested DS alloy, unloaded from 0.9% strain, showing dislocations have penetrated the γ′; see dislocations marked C. The γ′ has darker shade. Arrows such as A show the γ/γ′ interface and interface dislocations in the V channel. B shows interface dislocation network in a horizontal channel.

Fig. 8 is a TEM image of the above partially tested tensile specimen. Arrows such as A point to the γ/γ′ interface. The dislocations at these locations correspond to interface dislocations in the vertical channels. Interface dislocations may also be observed in regions marked B, and correspond to locations where the cross section just grazes the γ/γ′ interface. The arrows, such as at C, indicate super-dislocations of <110> type in the γ′ phase. The individual ½<110> dislocations are not resolvable in this image, but were confirmed by weak beam imaging. Such dislocations were absent in the untested material, and confirm that the γ′ phase has yielded after the elastic strain started to bend back at B in Fig. 6a.

3.2 Creep Test of DS Alloy at 900°C at 425 MPa

Fig. 9 shows the phase specific elastic microstrains in the [001] oriented γ and γ′ phase as a function of creep time at 900°C/425 MPa. The evolution of total macrosopic strain, measured by the extensometer, is also shown to aid our understanding of the deformation mechanisms. The initial value of macrostrain in the plot is arbitrary, being associated with the electrical zero point of the extensometer. The end of mechanical loading is indicated by point O. The macroscopic strain shows that the secondary creep stage started at point A at a creep strain of approximately 0.5%. This secondary creep stage transitioned to the tertiary creep stage at point B, at an accumulated creep strain of approximately 1.8 %. The sample failed at a total strain of 24%. In Fig. 9, R marks the elastic strain in the phases at zero load. This point is identified with zero elastic strain, although the γ and γ′ contain substantial initial misfit stresses. The points marked F correspond to elastic strains at zero load after failure.

A common characteristic of the plots in Fig.9 is that the elastic strains in the γ and γ′ phases rapidly reach steady state values. The slight increases that are observed after 1250 minutes is likely a result of reduced cross section and consequently higher applied stress, and is considered outside our scope of discussion.

In Figure 9, the steady state condition appears to coincide with the onset of secondary creep. On the other hand, the onset of tertiary creep does not appear to have any significant influence on

the elastic strains in the phases. In other words, simply by observing the elastic strains it is difficult to say whether a material is in secondary or tertiary creep.

Fig. 9(a) also shows that the γ and γ' phases start out with similar strain of 0.0045 (without correcting for misfit strain) at the beginning of creep. After 500 minutes, the elastic strain in the γ' phase increased to 0.005 while that for the γ phase dropped to 0.0034. This type of behavior indicates load transfer from the γ phase to the γ' phase, due to the creep of the weaker γ phase.
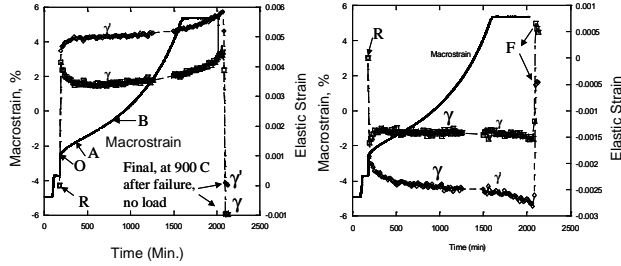

Figure 9. Macroscopic creep strain and the evolution of average elastic microstrain along the tensile (left) and transverse (right) direction of DS sample tested at 900°C/425 MPa.

The lattice parameters in the creep test can be used to calculate the lattice misfit versus creep time. The misfit in the loading and transverse directions are shown in Figures 10a and 10b, respectively. It may be noted that at failure (F) when there was no load in the specimen, the misfit in the loading direction is almost zero, in agreement with post-creep XRD measurements by Biermann et al [24,31]. However, rather than the end of the test, the misfit evolution in captured during the entire test.
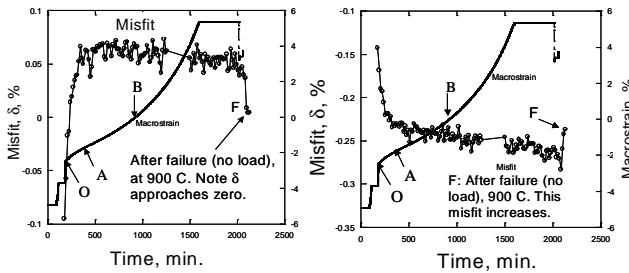

Figure 10. The evolution of misfit during creep of DS alloy at 900C/425MPa. (a) average misfit parallel, and, (b) perpendicular to loading direction.

Before interpreting these results, one may note that the change in misfit in the loading direction derives mainly from the horizontal (H) channel, because the vertical (V) channels are constrained by near isostrain conditions unless additional misfit dislocations are created to relieve misfit. Since the stress in the loading direction in the H-channel as well as the γ' is determined primarily by the applied load, the elastic strain in the loading direction in this channel can only change through a change in transverse stress in that channel (Poisson's effect). In other words, changes in misfit in Fig. 10a must reflect changes in transverse stress in the horizontal γ channel. Figure 10a shows that the misfit initially becomes more positive with creep time, suggesting that a_γ must reduce in the loading direction. This can only occur if the transverse stress becomes more positive in the γ phase in the horizontal channel. The scenario described here is in agreement

with published understanding of dislocations accumulation in the H and V channels, as illustrated in Figure 11 [23-27]. Thus, the dislocations on the horizontal face extend the γ phase in the H-channel in the transverse direction, with accompanying Poisson's contraction related decrease in 'a' of γ in loading direction. Thereby, the misfit becomes more positive with creep time, although Figure 10a shows that saturation is reached quite early.

With such geometrically necessary dislocation network in the H-channel, it also follows that misfit must become more negative in the transverse direction with creep time. In addition, the longitudinal strain in the V-channel is also reduced as tensile load is transferred from the V-channel to the γ' phase, thereby leading to a Poisson's expansion of the γ-phase in the transverse direction in the V-channel. Both these effects would lead to a net reduction of the misfit in the transverse direction, i.e., towards a larger negative misfit. Fig. 10b confirms that the increased negative misfit in the transverse direction is in agreement with experimental observations. In addition, the net changes in misfit after specimen failure (last data points), compared to the initial misfits are also in agreement with Fig. 11.
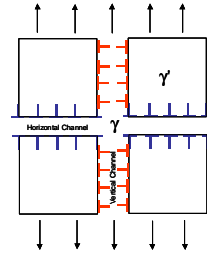

Figure 11. Sketch illustrating geometric dislocation buildup. The dislocations in the H-channel account for the constraint imposed by the strong γ' phase on the γ, as the latter stretches inelastically in the loading direction. In essence, the dislocations serve to increase the measured negative misfit in the transverse direction.

Microstructures of DS Alloy Samples Crept at 900°C

The above failed sample exhibited significant rafting, as well as the penetration of dislocations into the γ'; note that the strain was very high (24%) at failure. A second sample under identical creep conditions, but unloaded after 0.8% creep strain showed only interface dislocation structure. There were no signs of rafting or any evidence of dislocations cutting the γ' phase. A third sample unloaded after 3% creep strain showed evidence of rafting and only occasionally dislocations were observed cutting the γ'. Thus, rafting appears to be the dominant mechanism during creep under this test condition. A fourth sample was crept at 375 MPa at 900°C. This test showed onset of tertiary creep after about 1.5% creep strain, and it too exhibited early stages of rafting.

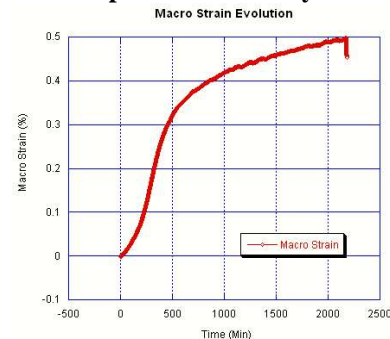### 3.2 Creep Test of SX Alloy at 1092°C at 120 MPa

Figure 12. Creep curve of sample tested at 1092C/120 MPa

The creep data in the low stress very high temperature regime is shown in Figure 12. This creep data at 1092 C/120 MPa is unusual in that the far-field creep strain exhibits an initial acceleration, before the response settles down to what resembles primary and secondary creep. The total creep strain is only about 0.5% after 37 hours. The elastic strain evolution is shown in Figure 13a and 13b. In these plots, the elastic strain is once again set at zero at the start of loading (R), although there is a misfit of approximately -0.003 at 1092 C. At the end of loading and following an additional 15 minutes (point A), the elastic strain is larger for the γ compared to γ'.

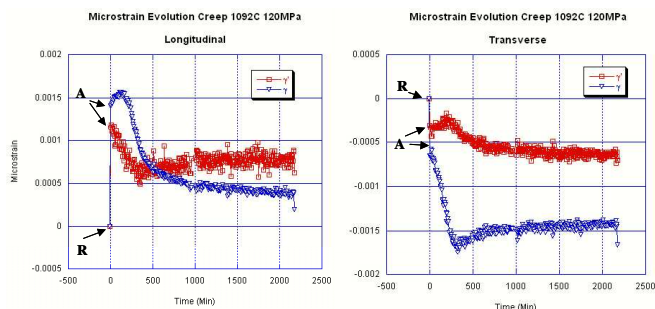Figure 13. Elastic strain evolution of SX PWA1484 alloy at 1092C/120 MPa. Square and triangle symbols represent γ and γ' data, respectively. Left: longitudinal, right: transverse strains.

Figure 13 is drastically different from the behavior observed for the sample tested at 900 C. Starting from the very beginning of creep, the elastic strain in the γ' in the loading direction decreases up to about 400 minutes, rather than an increase that is generally observed at the lower temperatures. Correspondingly, there is an initial increase in elastic strain in the γ-phase.
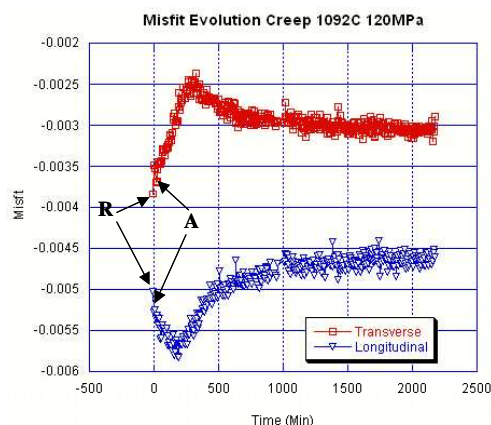

Figure 14. Misfit in longitudinal and transverse directions as a function of creep time at 1092 C/120 MPa.

Figure 14 shows misfit as a function of creep time for this sample. R marks the point of zero load at 1092 C while A refers to the first data point following completion of mechanical loading. Points A and R are reasonably close to each other, and confirms that elastic loading itself has little effect on the misfit. Indeed, during the tensile test there was no change in misfit up to 350 MPa. Thus, although the misfit is calculated with the specimen under load, changes in misfit can be interpreted in terms of changes in internal stress brought about by various factors, such

as the formation of interface dislocation structures. Fig.14 shows that the misfit in the loading direction initially becomes more negative with creep time. One way that this can happen is through a loss of tensile misfit stress in the γ' phase, which we estimate as approximately +150 MPa based on a misfit of -0.003 (see earlier section). A loss of misfit stress in the loading direction would become larger, thereby leading to an enhanced misfit with creep time. This is exactly what is observed in Fig.14.

The microstructure of the sample following creep is illustrated in Figure 15. It is clear that the microstructure is completely rafted at this stage, and is responsible for limiting the total creep to a small value of 0.005. Thus, in agreement with previous authors [25], a fully rafted structure can be good so long as the stress is low and the γ' rafts are not cut by dislocations.

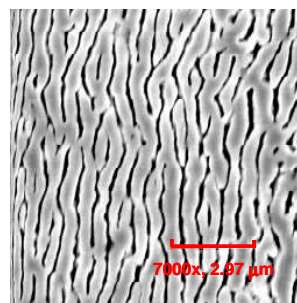
Figure 15. Microstructure of sample crept at 1092 C/120 MPa for approximately 37 hours. Loading axis is horizontal.

4. DISCUSSION

Before the start of the experiments, there was concern about the viability of the neutron diffraction technique to probe microstrains in DS and SX alloys. Fortunately, the experiments show that the rocking technique is able to overcome problems of specimen alignment, including possible loss of alignment due to specimen straining. In other words, a method to probe such materials has been established. Most importantly, the *in situ* neutron measurements provide a peek into the internal stress evolution that had hitherto not been possible.

Tension Test of DS Alloy at 900 C
The lattice parameters indicate very low misfit (~0.04%) at temperatures below about 750 °C. In addition, the lattice parameter of γ' at RT within the alloy and after the γ' precipitates were extracted from the superalloy were almost identical. Thus, as a first approximation, the RT lattice parameter of each phase may be identified with a stress free condition. Zero stress condition at RT was also suggested for a CMSX4 alloy [1]. With this as a basis, and assuming that subsequent changes in misfit are only due to different coefficients of thermal expansion (α) of each phase, the misfit stress in each phase can be estimated as a function of temperature and loading. In the analytical formulation, the precipitate and matrix are assumed to have identical elastic constants, and Figure 6 confirms that the difference in elastic constant between γ and γ' phase is indeed very small. In addition, the constituents are assumed to be isotropic. Although the anisotropic ratio ($A=2(S_{11}-S_{12})/S_{44}$) is as high as 2.7 (rather than 1), nevertheless for the purpose of calculating misfit stresses on the equivalent {100} planes in the <100> directions, the material behaves essentially as isotropic and elastic with $E = 1/S_{11}$, and

Poisson's ratio, $\nu = -S_{12}/S_{11}$. Here, the three S_{ij} are the independent compliance coefficients in the cubic material axes {100}<100>. Note that the thermal mismatch ($\Delta\alpha$) is not known *a priori*, but rather it has to be deduced from the overall misfit measurements at temperature. Thus, rather than conduct a series of FEM analysis with different assumed α for each phase, the formulas from the analytical method provides a direct estimate of the unconstrained thermal misfit ($\Delta\alpha\Delta T$), as well as the average mismatch induced stresses in the two phases.

In the case of cuboidal precipitates, it has been shown in [12] using Eshelby and Mori-Tanaka method that the constrained misfit, δ, can be related to the thermal mismatch as follows:

$$\delta = \frac{1+\nu}{3(1-\nu)}\Delta\alpha\Delta T \qquad (2)$$

where $\Delta\alpha = (\alpha_{\gamma'} - \alpha_{\gamma})$, $\Delta T = T - T_o$, T is any temperature, and T_o is a reference temperature. In this work, T_o is identified with RT (25 °C), and α_{γ} and $\alpha_{\gamma'}$ represent the unconstrained *secant* CTE of the phases between T_o and the temperature (T) of interest. Thus, $\Delta\alpha\Delta T$ can be obtained very easily from the measured misfit, δ. In the mechanical strain/stress calculations, the values of δ were reduced by 0.04% (see Fig. 5), in keeping with essentially zero stress assumption at RT.

The average tension stresses in each phase is [12]:

$$\langle\sigma\rangle_{\gamma'} = -(1-V_f)\frac{2E}{3(1-\nu)}\Delta\alpha\Delta T \qquad (3)$$

$$\langle\sigma\rangle_{\gamma} = V_f\frac{2E}{3(1-\nu)}\Delta\alpha\Delta T$$

Note that although the stresses in the γ phase are highly non-uniform, they are uniform throughout the γ' particle, in the spirit of Eshelby's analysis and also largely in agreement with FEM analysis using an eighth of the γ/γ' unit cell. Thus, the first of equation (3) is indeed a good representation of the actual normal stress in the γ' particle in any of the three <100> directions.

In our calculations, E and ν are based on Krivko's analysis [28], where the data for MAR M-200 alloy were expressed as: S_{11} = 0.7167x10^{-2} -0.2486x10^{-6}T+2.2848x10^{-9}T^2; S_{12} = - 0.2742x10^{-2} + 0.1766x10^{-6}T - 0.9999x10^{-9}T^2; S_{44} = 0.7709x10^{-2} + 0.5500x10^{-6}T+1.5106x10^{-9}T^2; where T is in degree Kelvin and S_{ij} are in GPa^{-1}. In this way we obtain the following values at 900 °C: (S_{11}=1.0091×10^{-5} MPa^{-1}, S_{12}=-3.91×10^{-6} MPa^{-1}, and S_{44}=1.04×10^{-5} MPa^{-1}, or, C_{11}=199.4 GPa, C_{12}=127.6 GPa, C_{44}=95.9 GPa;). The E_{001} calculated from Krivko's estimation (99.8 GPa) are in good agreement with our measured E_{001}=98 GPa at 900°C. The value of ν in [28] is 0.38 at RT, increasing only slightly to 0.39 at 900 °C and above. The ν from our stress strain curves in the elastic regime (Fig.9) was 0.46. This is a rather high value in the elastic regime, and is likely caused by the presence of multiple grain orientations in the transverse direction of the DS alloy, and so we have opted to use the more reasonable value of 0.39.

Using the measured constrained misfit δ of -0.001 between RT and 900 C, equation 3 provides average stresses of 50 MPa and -93 MPa for the γ' and γ phase, respectively. Independent anisotropic FEM calculation with the above S_{ij} and with input of $\Delta\alpha\Delta T$ = -0.0013 based on δ = -0.001 and equation (2), give average stresses of 54 MPa and -100 MPa for the γ' and γ phase, respectively. In addition, the δ calculated directly from the FEM results also works out to -0.001. The agreement in the average stress values between the analytical expression and FEM results are considered good, and justify our analytical assumptions.

The unit-cell FEM results show a large variation in the stress in the γ phase. In the highly constrained regions of the γ phase (i.e., regions away from the corners of the γ' cube), the stress in the γ channel parallel to the interface is -206 MPa. Figure 16 illustrates that this misfit induced stress (σ_m) in the horizontal channel complements the applied tensile stress to increase resolved shear stress (RSS), and thereby initiates dislocation motion inside the γ phase. On the other hand, slip in the vertical channel has to depend completely on the applied load, and so inelastic deformation will be initiated only at a larger stress. The elastic strain data for the γ phase exhibits linear behavior up to 350 MPa (Figure 6). Beyond this stress, the γ-curve exhibits a concave up behavior indicating that it is unable to pick up any further load, while the γ' phase exhibits a concave-down behavior, indicating that γ' starts to take up additional load from the γ phase. Thus, we believe that the saturation of elastic strain in the γ phase above $\sigma_a = 350$ MPa is due to the attainment of the critical resolved shear stress (CRSS) in the V-channel. The CRSS in the H-channel is of course reached much earlier, but the measured extensometer strain was extremely small because the glide of dislocations was restricted to the H-channel. This is consistent with no visible non-linearity in γ elastic strain below 350 MPa.
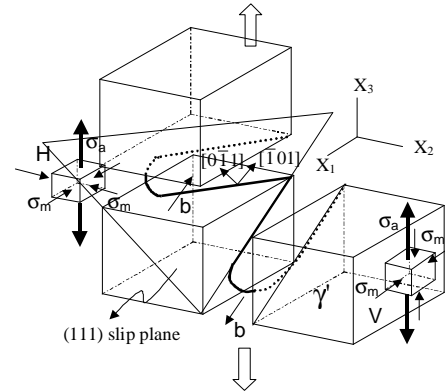

Figure 16. Sketch of dislocation lines showing slip through the γ-channels on the $(111)[\bar{1}01]$ system. The small cubes depict state of stress in the γ-channels, comprised of compressive in-plane misfit stresses (σ_m) and the applied stress (σ_a).

We can calculate the RSS in the two γ-channels using the critical applied stress of 350 MPa in Figure 6, and a biaxial compressive stress of -206 MPa parallel to the interface. Thus, referring to Figure 16, the RSS for {111}<110> slip on the H and V channels are given by:

$$\tau_{RSS}^H = (\cos 45)(\cos 54.74)(\sigma_a + \sigma_m) = \{\frac{1}{\sqrt{6}}(350+206)\} = 227\,\text{MPa} \qquad (4)$$

$$\tau_{RSS}^V = (\cos 45)(\cos 54.74)\{(\sigma_a - \sigma_m) + \sigma_m\} = 143\,\text{MPa}$$

where we have used $\sigma_a = 350$ MPa and $\sigma_m = 206$ MPa.

Since dislocations must glide on both channels for measurable plastic strains in the tension test, the CRSS of the γ phase must be the smaller of the two RSS, namely *143 MPa*. The CRSS of the bulk γ phase (from a solid solution alloy) is approximately 52 MPa [29]. Thus, the large three-fold difference in CRSS illustrates that the γ phase is locally strengthened.

The observed strengthening of the γ phase is believed to be the large contribution from Orowan bowing of dislocations loops

as they first enter and then travel through the γ channels. The bowing radius of the screw segments in the γ channels is dictated by the channel width, l. As shown by Pollock and Argon [1], the Orowan stress (τ_{orowan}) can be calculated as follows:

$$\tau_{Orowan} = \mu b / l = \mu a / h\sqrt{3} \qquad (5)$$

where μ is the shear modules, a the lattice parameter of the γ phase, b the Burgers vector of the glide system, l the width of the γ channels in the glide plane, and h the width of γ channel in the [001] direction. Using typical data, we estimate the Orowan stress as 131 MPa, in which $\mu = 45.2$ GPa, $a=0.364$ nm, and $h=70$ nm are used. The value of μ is based on applying only a shear stress on the $(111)[0\bar{1}1]$ system in the crystal and calculating the corresponding elastic shear strain. The ratio of the shear stress to this strain is estimated as μ, which may be expressed as $\frac{1}{\mu} = \frac{S_{44} + 4(S_{11} - S_{12})}{3}$, or μ = 45.2 GPa for the S_{ij} used in our analysis. This value is consistent with 43.5 GPa used in [21. The additional factor that resists dislocation motion is the friction stress from solid solution, which we estimate as 18 MPa based on [1]. Thus, we obtain a RSS of 149 ±20 MPa, where the bounds incorporate error in channel width measurement (±5 nm) and estimation of friction stress (~10 MPa) based on [1]. The experimental CRSS is 143 MPa, where we estimate an error of ±10 MPa stemming from inaccuracy in misfit stress estimation in the highly constrained zone of the γ-channel. Our primary conclusion is that the measured CRSS of the γ phase is in reasonably good agreement with Orowan stress, and provides a first *in situ* validation that glide of dislocations in the γ channels is controlled by Orowan bowing. We believe this is an important outcome of the experiments and provides confidence that Orowan stress calculations can be utilized to analyze creep of superalloys.

It is interesting to postulate about the lowest applied stress at which creep can occur, where this stress is just large enough to allow dislocations to bow into the H-channel. Recall that glide is a requirement for any dislocation creep. The value of RSS in the h-channel is $\left(1/\sqrt{6}\right)*(\sigma_a + \sigma_m) = 0.408*(\sigma_a + 206)$. Equating this to the CRSS of 143 MPa, the required applied stress is (350-206) = 145 MPa. One may consider this stress as a "threshold stress" for creep of the superalloy. Tests on CMSX-3 [2] showed that the creep strain was less than 10^{-5} at 900 °C after 158 hours at 110 MPa. Thus, the threshold stress is at least as high as 110 MPa. The misfit stress was higher in their case and the V_f was 0.7. At 850 °C, creep was less than 10^{-5} after 228 hours at 130 MPa. Overall, we consider the agreement between the threshold stress and required RSS in the horizontal channel as reasonable.

The sharp bendback at 600 MPa of the γ′ phase (Point B in Figure 6a, elastic strain = 0.0069) indicates a sudden loss of elastic strain. This point indicates that the dislocations begin to penetrate γ′. The TEM micrograph in Figure 8 also confirms dislocation entry into γ′. Similar bendback was also noted for a tensile tested polycrystalline CM247LC sample at RT [11].

In order to calculate CRSS of γ′ phase, we use the equations:

$$\sigma_{001}^l = C_{11}\varepsilon_{001}^l + 2C_{12}\varepsilon_{010}^t$$
$$\sigma_{010}^t = C_{12}(\varepsilon_{001}^l + \varepsilon_{010}^t) + C_{11}\varepsilon_{010}^t \qquad (6)$$
$$\tau_{CRSS}^{\gamma'} = \left(\frac{1}{\sqrt{6}}\right)\left(\sigma_{001}^l - \sigma_{010}^t\right)$$

where ε^l and ε^t refer to longitudinal and transverse elastic strain, respectively, in the γ phase at point B. Figures 6a and 6b indicate

that these strains are 0.0069 and –0.0034, respectively. However, these strains were measured with respect to the zero load condition at 900 °C, when significant stresses are present in both the γ and γ′ phases. The total mechanical strain must also include the contribution from thermal misfit. In this way, the misfit induced mechanical strain in γ′ at 900 °C is 0.0001573. We thus obtain the longitudinal and transverse strains in the γ′ phase as 0.0070573 and –0.0032427, respectively, at point B. Using the elastic constants, we obtain a CRSS of 302 MPa for γ′ at 900°C.

For comparison, the CRSS of the bulk γ′ is reported to be about 189 MPa at 900 °C [29]. This value is far below the value of 302 MPa measured in this investigation by *in situ* neutron diffraction technique. One reason for the higher CRSS of the γ′ phase is the difficulty of entry of dislocations from the γ phase into the γ′ phase. In [30], shearing of γ′ has been observed through pairs of a/2<110> dislocations in the γ phase, which then propagate as a super dislocation in the γ′ phase. The associated RSS can be estimated using the formula:

$$\tau = \Gamma / 2b \qquad (7)$$

where Γ is the antiphase boundary (APB) energy and b is the Burgers vector $a/\sqrt{2}$. In [36] we have estimated the APB in the γ′ as 150 mJ/m^2 ± 20mJ/m^2. Using 150 mJ/m^2, we obtain CRSS of 279 MPa for the γ′ phase. This is less than the experimental 302 MPa, but the agreement is considered reasonable.

Creep Test Results

The creep data for the DS alloy at 900 C shows that tertiary creep starts at a creep strain slightly larger than 1%. However, the microstrains from the creep test (Fig. 9) do not reveal any specific feature that may indicate the transition from secondary to tertiary creep. If the elastic γ′ had transitioned to large scale creep deformation, then a drop (bendback) in the elastic strain in the γ′ should have been noticeable, similar to the tensile test (Fig. 6a). Unfortunately, there is no such indication in Fig. 9. In addition, plugging the elastic strains in equation 6, the RSS in the γ′ at the onset of tertiary creep is 217 MPa, which is less than the CRSS of 302 MPa from the tension test. Tertiary creep was also observed at 375 MPa, when the RSS was 191 MPa. These observations suggest that γ′ cutting may not be the mechanism responsible for tertiary creep under moderate stress at 900 C. While there still remains the difficulty of reconciling this conclusion with observed dislocations in γ′, we note that dislocations were relatively few and may not explain the large strain rates under tertiary creep.

The mechanism that seems plausible for the onset of tertiary creep is rafting. Rafting was only partial, so that many vertical paths were available for dislocations to find a passage between rafts and cutting was no longer necessary for slip propagation. While rafting is more common at higher temperatures and longer times, it has been observed in CMSX-4 at 950 C [25]. Rafting is driven by the difference in strain energy of the vertical and horizontal channels [5,6]. Among various factors, the lattice misfit plays an important role. In this regard, it is interesting to note that the longitudinal misfit shows a decreasing trend, albeit small, at about the time tertiary creep initiated (Fig. 10).

FEM simulation of creep that is not detailed here, whereby there is power law creep of γ and only elastic deformation of γ′, show that the overall creep curve should concave slightly downwards, rather than concave up as with tertiary creep. In spite of this inadequacy of FEM simulation, the analysis does indicate that if inelasticity is confined to the γ channels, then with time the longitudinal stress (along tensile axis) in the V-channel will

decrease while the longitudinal stress in the γ′ will increase. In addition, the H-channel will develop a transverse tensile stress. This secondary stress can be explained physically by the constraint imposed by the γ′, which prevents the γ in the H-channel to contract laterally while it extends longitudinally. These results are consistent with the dislocation arrangement shown in Fig. 11.

It is instructive to view the dislocation network in the context of what normally happens at an initially coherent interface. Thin film analysis and observations indicate that if the elastic energy associated with misfit is high, then an interface dislocation network can form as shown in Fig. 17a, such that the interface becomes semi-coherent. The extra half plane is created in the phase with smaller lattice parameter, and the misfit stress is relaxed in each phase; i.e., each phases relaxes to its unconstrained lattice spacing. If it were possible to determine the misfit in the horizontal direction by measuring lattice parameters, then the unconstrained condition would yield a larger magnitude of misfit $\{2(b1-b2)/(b1+b2)\}$ than in the initially constrained state. In the context of the superalloy, such a relaxation at temperature would lead to the misfit dislocation network shown in Fig. 17b. The dislocation network on the H-channel is identical to Fig.11. On the other hand, the dislocation network on the V-channel is opposite to that in Fig. 11.
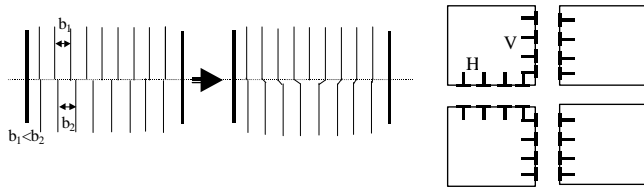

Figure 17. (a) Misfit dislocations that form in thin films to relieve misfit stresses. (b) The type of misfit dislocations that would lead to reduction in misfit stress in the γ/γ′ system.
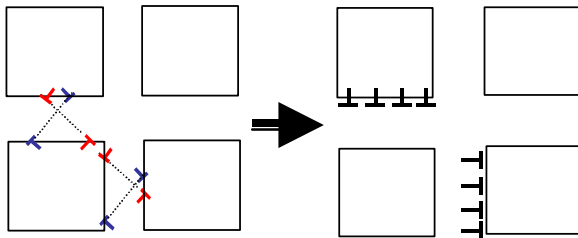

Figure 18. (a) Slip dislocations depositing on horizontal and vertical interfaces. (b) Equivalent arrays of dislocations resulting from reaction of dislocations on the two slip systems in (a).

The difference can be explained by referring to Fig.18. The dislocations moving in the H-channel contribute to a lateral contraction of the γ′ and a dilatation of the γ. Thus, these slip induced dislocations serve the same purpose as a thin-film misfit induced dislocation network (Fig. 17). Essentially, the extra-half plane in the γ′ serves to relax the misfit stresses. At the same time, this relaxation serves to enhance the negative misfit measured in the transverse direction. The latter is in full agreement with Fig. 10b. On the vertical interface, the slip dislocations are opposite to that for a misfit dislocation network. The expansion of the γ′ and contraction of γ in the loading direction due to slip dislocations

serve to match the lattice on either side; i.e., reduction in the magnitude of misfit. The creep at 900 C (Fig. 10) shows that after failure, when there is no applied stress, the measured misfit in the loading direction is reduced to almost zero.

At 1092 C we observe the rather unexpected behavior in Fig. 13, where the longitudinal elastic strain in the γ′ decreases at the beginning, accompanied with an increase in its transverse strain. In other words, the γ′ appears to lose load. The only plausible explanation that appears to be consistent with this observation is that actual misfit dislocations, of the type in Fig. 17b, deposit rapidly on the vertical walls. Indeed, the decrease in longitudinal elastic strain in γ′ in Fig. 13 agrees with our estimate of elastic strain due to loss of misfit stress in γ′. This behavior, we suggest, may likely be aided by the contribution of applied stress, such that the work input aids the misfit-dislocation induced relaxation process. This type of misfit dislocation does not deposit on the horizontal faces likely because slip dislocations play the role of actual misfit dislocations in relaxing misfit stresses. In turn, the loss of misfit stress in γ′ along the tensile direction requires that additional stress be borne by the γ V-channel, leading to faster creep rate. This may explain the initial acceleration of the creep test at 1092 C. Thus, both the macroscopic creep data and the microstrain data are consistent with a loss of longitudinal misfit stress through formation of interface dislocation network. The effect also manifests as an initial decrease in misfit along the loading direction, as observed in Fig. 14. However, with time, as slip dislocations are deposited, the γ′ is stretched longitudinally, and misfit progresses towards a less negative value (Fig. 14).

The importance of misfit dislocations is that they contribute to loss of coherency, making the interface an easier source or sink for vacancies. Thus, such dislocations set the stage for mass transfer and rafting. It would be interesting to know if rafting was completed by the time steady state conditions were established at 1092 C (~ 750 minutes). The onset of the decrease in longitudinal misfit in Figure 10a (900 C) also appeared to coincide with gradual transition to tertiary creep, considering that rafting was observed in that sample. While the explanations provided in the above two paragraphs appear most consistent with experimental data, additional experiments and analyses are needed to confirm the actual mechanisms.

The additional mechanism that perhaps should be considered, particularly in the range 900 - 1100 C, is that of interface sliding because of dislocation induced loss of coherency at the γ/γ′ interface. Experimental efforts at observing sliding has not been successful to date. However, we are currently conducting FEM modeling work that incorporates sliding as a possibility, and comparison between our phase strain evolution and those calculated by FEM is expected to provide some quantitative measure of the role of interface sliding during creep.

5. CONCLUSIONS

The following conclusions can be drawn from this work:

(1) A rocking technique can be successfully utilized during *in situ* neutron diffraction of DS alloys and single crystals, to accurately monitor elastic strains in the coherent γ/γ′ phases at high temperatures.
(2) The misfit remains essentially zero from RT to about 750 °C, after which it increases more rapidly to about -0.10% at 900 °C. This type of onset of rapidly changing misfit has been observed in

other alloys, and it approximately coincides with the temperature at which maximum tensile strength is reached for the alloy.

(3) From the analysis of the elastic strain data during the tensile test at 900 C, the CRSS of the γ phase is estimated to be around 140 MPa, which is in good agreement with the Orowan bowing stress. Thus, the data provides a first *in situ* direct confirmation of the validity and importance of the Orowan bowing calculations.

(4) The insitu measurements provide insight on the internal stress evolution with creep time, which had not been available earlier. However, the elastic strains in the creep test at 900 C do not provide any indication of cutting of γ′ at the onset of tertiary creep. The elastic strains reach near steady state in the secondary regime, and the resolved shear stress in the γ′ always remains below the CRSS measured from the tension test at 900 C. Samples tested to 3% strain or failure show strong evidence of rafting, indicating rafting may be the primary contributor to tertiary creep. Although dislocations were also observed inside γ′, their presence cannot be explained by the estimated RSS, and may involve additional mechanisms of cutting.

(5) The initial creep stage 1092 C/120 MPa shows a number of unanticipated features, such as an initial acceleration of creep, accompanied with a steady decrease in γ′ longitudinal strain. A preliminary explanation is provided in terms of the deposition of misfit dislocations preferentially on the vertical channels.

6. ACKNOWLEDGEMENT

7. REFERENCES

1. Pollock TM, Argon AS. Acta Metall Mater 1992;40:1-30.
2. Pollock TM, Argon AS. Acta Metall Mater 1994;42:1859–74
3. Matan N, Cox DC, Rae CM, Reed RC. Acta Mater 1999;47:2031-2045
4. Buffiere JY, Ignat M. Acta Metall Mater 1995;43:1791–7.
5. Nabarro FRN. Metall Mater Trans A 1996;27:513–30.
6. Ohashi T, Hidaka K, Imano S. Acta Mater 1997; 45:1801-10.
7. Epishin A, Link T. Superalloys 2004, Seven Springs, PA: editors Green KA, Pollock TM and Harada H, TMS; 2004: 849-858.
8. Srinivasan R, Eggeler GF, Mills ME, Acta Mater 2000; 48:4867-4878.
9. Link T, Epishin A, Bruckner U, Portella P. Acta Mater 2000;48:1981-84.
10. Cahn RW, Haasen P. In: Physical Metallurgy Part 1. 2nd Edition, Elsevier Science Publishers, BV, 1983, p.662.
11. Ma S, Rangaswamy P, and Majumdar BS. Scripta Mater 2003; 48:525-31.
12. Ma S, Brown D, Bourke MAM, Daymond MR, Majumdar BS. Mater Sci Eng A 2005;399:141-53.
13. Ma S, Seetharaman V, Majumdar BS. Under review at Acta Mater. 2004.
14. Rietveld, H.M., *J. Appl. Crystallogr*, **2**, 65 (1969)
15. Larson AC and Von Dreele RB. General Structure Analysis System (GSAS), Los Alamos National Laboratory Report LAUR, 86-748, 1994
16. VonDreele RB, J. Appl. Crystallography 1997; 30: 517
17. Bacon GE, Neutron Diffraction, Oxford at the Clarendon Press, 1962
18. Watanabe R, Kuno T. Trans. ISJJ; 1976; 16: 437-440.
19. Caron, P. Superalloys 2000, TMS Publications, 2000
20. Volek A, Pyczak F, Singer RF, Mughrabi, H, Scripta Mater 2005; 52: 141-145
21. Lu Y, Masters Thesis, Materials and Metallurgical Engineering Department, New Mexico Tech, Socorro, NM 87801: 2006
22. Saunders A, Guo Z, Li X, Miodownik, Schille J Ph, Superalloys 2004, Seven Springs, PA: editors Green KA, Pollock TM and Harada H, TMS; 2004: 849-858.
23. Carry C, Strudel JL. Acta Metal 1977;25:767-77.
24. Kuhn HA, Biermann H, Ungar T, Mughrabi H. Acta Metal. Mater 1991;39: 2783-94.
25. Mughrabi H, Tetzlaff U. Advanced Engineering Materials 2000;2:319-26.
26. Li J, Wahi RP. Acta Metal Mater 1995;43:507-17.
27. Ohashi T, Hidaka K, Saito M. Mater Sci Eng 1997;238A:42-9.
28. Krivko A I, Epishin A, Svetlov I, Samoilov A. Problemy Prochnosti (Problems of Strength) 1988; Issue 2:68-75.
29. Kear BH, Pope DP. In: Tien JK, Caulfield T, editors. Superalloy, Super-Composites and Superceramics. Boston:Academic Press; 1989. p.564.
30. Caron P, Khan T, Phil. Mag 1988: 54:859
31. Biermann H, Strehler M, Mughrabi H, Metall.Trans 1996;27A:1003-1014